Matter

CellPress

Article

Heavy metal removal using structured sorbents 3D printed from carbon nanotube-enriched polymer solutions

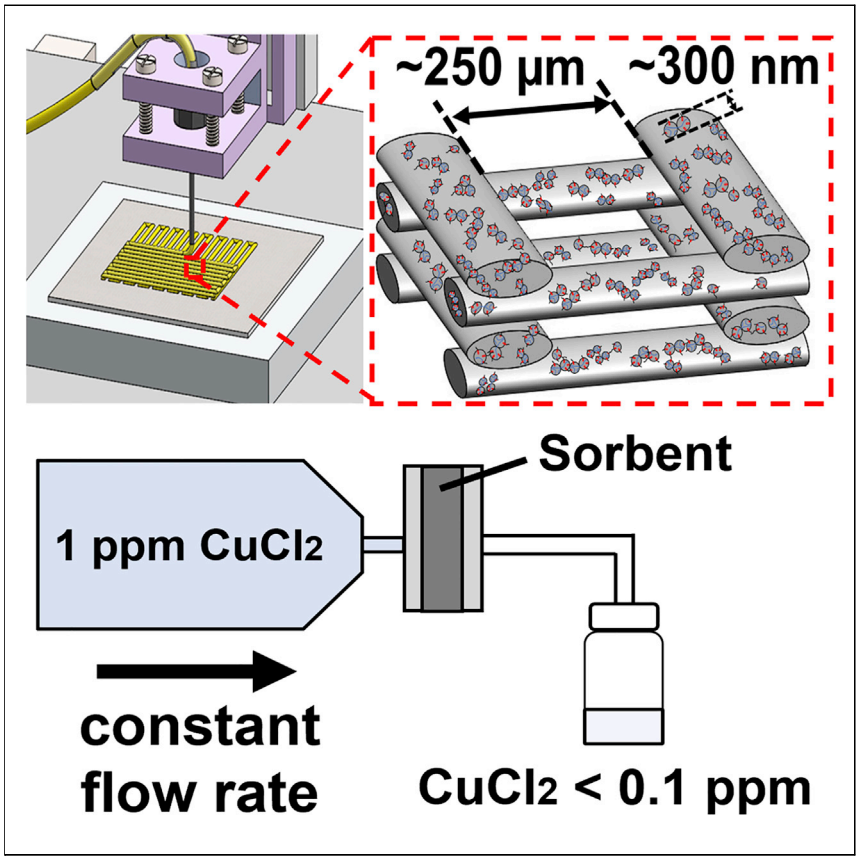

Hierarchically structured sorbents are fabricated using a combination of direct-ink-writing 3D printing and an *in situ* vapor-induced phase separation process. The approach is enabled by the increased pinching times arising from the inclusion of carbon nanotubes in the formulation of polymer composite inks. The resulting ability to control material structure across multiple length scales enables sorbents that are highly permeable, exhibit high binding capacity and selectivity, and effectively remove trace levels of metal ions under dynamic flow conditions.

Demonstrate
Proof-of-concept of performance with intended application/response

Jialing Xu, Cheryl Slykas, Adam S. Braegelman, ..., Matthew J. Webber, Vivek Sharma, William A. Phillip

wphillip@nd.edu

Highlights

Carbon nanotube-enriched polymer inks enable 3D printing of structured sorbents

Nanoscale sorbent architecture arises from phase separation in a humid environment

Facile reactions tailor the sorbent surface chemistry for target applications

Structured sorbents have high permeability, binding capacity, and metal ion affinity

Xu et al., Matter 5, 1–20
October 5, 2022
https://doi.org/10.1016/j.matt.2022.07.012

Please cite this article in press as: Xu et al., Heavy metal removal using structured sorbents 3D printed from carbon nanotube-enriched polymer solutions, Matter (2022), https://doi.org/10.1016/j.matt.2022.07.012

Matter

CellPress

Article

Heavy metal removal using structured sorbents 3D printed from carbon nanotube-enriched polymer solutions

Jialing Xu,[1] Cheryl Slykas,[2] Adam S. Braegelman,[1] Kevin Gabriel Alvarez,[1] Thomas Kasl,[1] Bryan W. Boudouris,[3] Matthew J. Webber,[1] Vivek Sharma,[2] and William A. Phillip[1,4,*]

SUMMARY

Sorbents with structures tailored at the molecular through device scales are needed to meet the demand for separations that can isolate trace analytes from complex mixtures. Here, direct-ink-writing three-dimensional (3D) printing is combined with a surface-segregation and vapor-induced phase separation (SVIPS) process to create hierarchically structured sorbents that satisfy this criterion. Composite inks containing polysulfone, polystyrene-*block*-poly(acrylic acid) (PS-PAA), and carbon nanotubes (CNTs) were formulated to allow these processes to proceed simultaneously. Enriching the inks with CNTs modulated their rheological characteristics such that microstructured sorbents with permeabilities of $\sim 10^5$ L m^{-2} h^{-1} bar^{-1} could be printed. The SVIPS process generated an interconnected network of PAA-lined nanopores whose chemistry was tailored to produce sorbents that recovered Co^{2+} selectively from mixtures of Co^{2+} and Li^{+} and efficiently treated sub-parts per million feed solutions under dynamic flow conditions. The versatile combination of 3D printing and SVIPS provides new strategies for manufacturing next-generation sorbents with structures controlled across multiple length scales.

INTRODUCTION

Developing separations processes capable of isolating dilute solutes from solution is essential to enabling the efficient removal of trace contaminants from drinking water, mining critical materials from non-traditional sources, and purifying therapeutic drugs in a cost-effective manner.[1–9] Adsorptive separations are uniquely well suited for these applications. However, shortcomings in materials design must be addressed to empower the fabrication of devices that meet the needs of emerging separations. Traditionally, adsorption is executed using packed beds filled with porous beads that provide high capacities for the capture of target solutes.[10–12] However, this operating configuration is hindered by mass transfer limitations that arise as the analyte diffuses from the outer surface of the beads into their porous structure, where the majority of active binding sites reside. Membrane sorbents are an alternative operating configuration that address the diffusive mass transfer limitations of packed beds.[13–15] Unfortunately, membranes are thin and offer limited capacity for solute capture. Enhanced mass transfer rates and increased binding capacities can be achieved by reducing the diameter of the porous beads or membrane pores, yet this approach will inevitably increase the resistance to flow, reducing throughput or requiring higher operating pressures.[16–18] Structured sorbents represent one promising approach to overcoming this trade-off between permeability and

PROGRESS AND POTENTIAL

Adsorptive materials are well suited for the separation processes needed to ensure a sustainable future (e.g., purifying drinking water, recovering critical minerals). Methods to transform these materials into sorbents with structure controlled at the nanometer through micrometer scales are necessary to translate lab-scale discoveries into practical devices. This study reveals that enriching polymer solutions with carbon nanotubes enables sorbents with hierarchical organization across scales to be 3D printed. Nanoscale phase separation of the polymer endows the sorbents with high capacity for solute capture. Moreover, sorbent chemistry can be tailored using facile reaction schemes. The use of these sorbents to remove heavy metal ions from water demonstrates the high affinity, capacity, and throughput necessary for a functioning technology. The versatility of the approach further expands the library of materials that can be used to fabricate separation devices from advanced materials.

capacity that hinders state-of-the-art sorbents. By controlling structure across several length scales, large channels that increase throughput can be introduced within a mesoporous matrix that endows the sorbent with structural stability and large surface areas for solute binding.[19–25]

Methods for producing structured sorbents are still nascent, but additive manufacturing has revealed promising technologies (e.g., fused deposition modeling, inkjet printing, digital light processing, laser melting) capable of fabricating devices with well-controlled structures at the nanometer through meter scales.[26–28] These techniques have enabled the fabrication of sorbents with high permeability, improved pore accessibility, and robust mechanical properties.[29–32] The resulting microstructures can tailor the flow path of the mobile phase to increase residence times and induce secondary flows that enhance mass transfer rates without reducing permeability.[33,34] For example, gold nanoparticles could be blended with sodium alginate to 3D print sorbents for the capture and degradation of organic dyes.[31] Another example demonstrating the benefits of printed polymer scaffolds used a polymer of intrinsic microporosity, PIM-1, with larger channels to regulate the flow of vapor through the sorbent. The sharp breakthrough curve exhibited in toluene vapor capture exemplified the effective mass transfer structured sorbents can provide in gas separation processes.[32] These initial examples demonstrate the promise of structured sorbents. However, realizing the potential of this approach for liquid phase separations requires the development of platforms that possess fully interconnected mesoporous matrices to increase capture capacity and material chemistries that can be modified to address the diversity of target solutes that are encountered.

Nonsolvent induced phase separation (NIPS) processes are a well-established method for generating porous polymer architectures (e.g., in membranes).[35–39] These processes are often implemented by casting a homogeneous polymer solution in the desired form factor and then exposing the solution to a nonsolvent environment. As the solvent and nonsolvent exchange, the solution phase separates to form polymer-rich and polymer-lean phases that template the solid matrix and the porous structure, respectively. Controlling for the composition of the solution, the mechanism used to introduce the nonsolvent plays a decisive role in controlling the nanostructure of the resulting material. For example, plunging a solution directly into a water bath can lead to rapid solvent-nonsolvent dynamics that have been implicated in the formation of macrovoids that compromise the integrity and performance of the polymer. However, exposing the same polymer solution to a humid environment slows the transfer of nonsolvent (i.e., water) into the solution, thereby suppressing the rate of phase separation and promoting the formation of interconnected, spongy nanostructures that possess high surface area per volume.[40–42] In addition to providing structural control, phase separation processes can be designed to tailor the functionality lining the porous polymers. For example, amphiphilic block polymers can be included in the casting solution such that during the phase separation process, the block with the higher affinity for the nonsolvent segregates to the interface between the two phases. If properly chosen, this block can impart target functionality to the material. On this basis, Zhang et al. developed a surface-segregation and vapor-induced phase separation (SVIPS) technique to develop composite polysulfone (Psf) polystyrene-*block*-poly(acrylic acid) (PS-PAA) membrane sorbents.[43] The PAA brushes that lined the surface of these membranes could be tailored post-synthetically to increase the binding capacity and affinity toward heavy metal ions.

In this study, we combine solution-based direct-ink-writing (DIW) 3D printing with a SVIPS process to address the need for hierarchically structured sorbents that can

[1]Department of Chemical and Biomolecular Engineering, University of Notre Dame, Notre Dame, IN 46556, USA

[2]Department of Chemical Engineering, University of Illinois at Chicago, Chicago, IL 60608, USA

[3]Charles D. Davidson School of Chemical Engineering and Department of Chemistry, Purdue University, West Lafayette, IN 47907, USA

[4]Lead contact

*Correspondence: wphillip@nd.edu

https://doi.org/10.1016/j.matt.2022.07.012

Please cite this article in press as: Xu et al., Heavy metal removal using structured sorbents 3D printed from carbon nanotube-enriched polymer solutions, Matter (2022), https://doi.org/10.1016/j.matt.2022.07.012

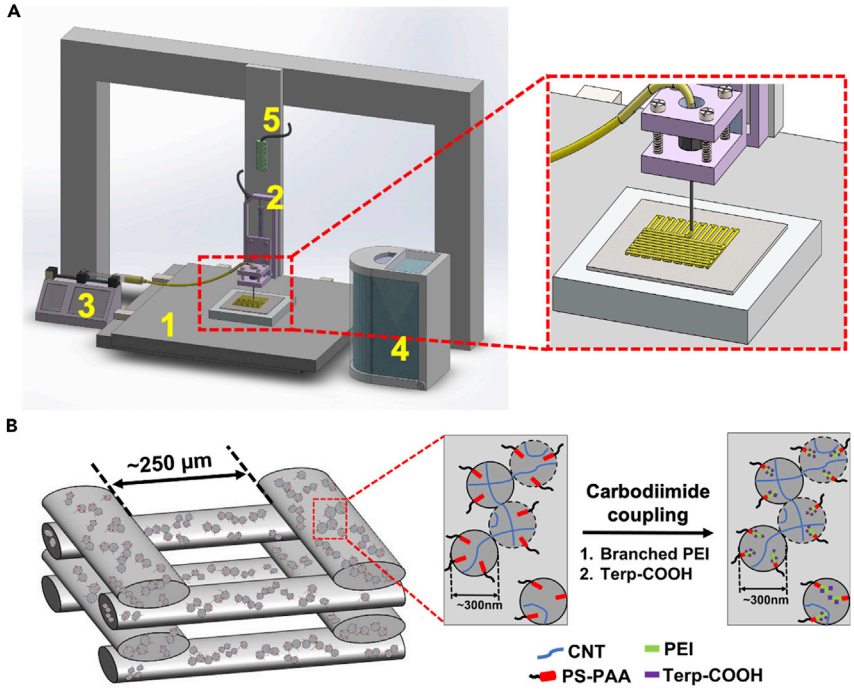

Figure 1. Fabrication of structured sorbents

(A) An overview of the direct-ink-writing printer used to fabricate hierarchically structured sorbents. The x-y stage (1) and z-axis controller (2) were programmed to control the position of a dispensing needle relative to the printing platform. The deposition of polymer composite ink onto the platform was controlled by a syringe pump (3). The deposition process occurred within a chamber whose humidity was measured and controlled by a humidifier (4) and humidity sensor (5).

(B) A schematic representation of the sorbent structure. The deposition of the filaments was controlled to produce woodpile structures with a micrometer-scale channel in the center of the filaments. Nanoscale pores formed throughout the filaments due to the SVIPS process initiated by the humid atmosphere. Polyacrylic acid (PAA) brushes that line the porous surface of the filaments enable the post-fabrication modification of the sorbent chemistry with poly(ethyleneimine) (PEI) and terpyridine-COOH (Terp-COOH) via sequential carbodiimide coupling reactions.

be deployed to isolate dilute contaminants and resources. Polymer composite inks are formulated to exhibit rheological responses that enable control over the sorbent microstructure through 3D printing. Simultaneously, the solution thermodynamics of these composite inks are designed to be consistent with the SVIPS process such that, as the solution is printed, it nanophase separates to form the fully interconnected porous network of the sorbent. Through facile post-synthetic coupling reactions, the sorbents are tailored to recover transition metal ions from sub-parts per million (ppm) concentration solutions. This combined technique demonstrates a straightforward method for controlling sorbent structure and chemistry across multiple length scales relevant to emerging separation process demands.

RESULTS AND DISCUSSION

Enriching composite inks with carbon nanotubes (CNTs) enables printing of microstructured sorbents

The DIW printer shown schematically in Figure 1A provides control over the microstructure of the sorbents. A 25-G dispensing needle (inner diameter 260 μm), connected to a syringe pump operating at a flow rate of 0.04 mL min^{-1}, was used to deposit polymer composite ink onto non-woven polyester substrates. The x-y

Please cite this article in press as: Xu et al., Heavy metal removal using structured sorbents 3D printed from carbon nanotube-enriched polymer solutions, Matter (2022), https://doi.org/10.1016/j.matt.2022.07.012

position of the needle was fixed, while its height above the printing platform was manipulated using a z-axis controller. The non-woven substrate was secured to an x-y planar controller that manipulated the position of the substrate relative to the dispensing needle. The platform moved at a linear velocity of 5 cm s^{-1} in the x and y directions as the filaments were being deposited. Woodpile structures 2 × 2 cm in size were generated by printing 40 filaments with a 250-μm gap between the filaments (Figure 1B). After one layer of the structure was deposited, the z-axis controller moved up 10 μm and the subsequent layer of filaments was deposited with an orientation perpendicular to the prior layer. This sequence was repeated until the desired number of layer numbers were reached. The whole filament deposition process occurred within a controlled humidity chamber to promote the SVIPS process.

The polymer composite ink, which consisted of 10% (by weight) Psf, 2% PS-PAA, and 0.1% CNTs dissolved in 2-pyrrolidinone (2P), was designed to produce filaments with nanostructured porosity. 2P was used as a solvent because it dissolves both the Psf and PS-PAA and it is miscible with water. The miscibility of 2P and water was a critical design feature as it allows water vapor from the environment to initiate the SVIPS process. The concentrations of Psf and PS-PAA, which were selected based on prior work, resulted in viscous solutions that could be extruded through the dispensing needle. However, at these polymer concentrations, the solution needed to be enriched with carbon nanotubes to print continuous, discrete filaments. As shown in Figure S1, using inks that did not contain CNTs resulted in the formation of large droplets at the tip of the needle as well as filaments that aggregated into granular particles. The need for enriching the polymer solution with CNT is attributed to the impact of the CNTs on the rheological properties of the composite ink.

As shown in Figure 2A, the steady shear viscosity of the composite ink containing 0.1% (by weight) CNTs was comparable to the viscosity of the CNT-free ink over the range of shear rates examined. Figure 2B features image sequences acquired by dripping-onto-substrate (DoS) rheometry protocols using a time step of Δt (s). The snapshots revealed that even though the 0.1% CNT and CNT-free inks had a matched shear rheology response, the liquid neck pinched more quickly for the CNT-free ink, leading to the extrusion of droplets rather than continuous liquid filaments. The minimum neck radius obtained by analyzing time series of DoS images are also plotted in Figure 2B. Slower pinching and delayed pinch-off are clearly visualized with increasing CNT concentration. The dashed lines display linear fits to the radius evolution data in the last stage, implying that pinching dynamics exhibit the terminal, viscoelastocapillary behavior associated with rate-independent steady, terminal extensional viscosity.[44,45] Increasing the CNT concentration to 0.2% led to a more pronounced shear-thinning response as well as substantial increases in the extensional viscosity and pinching time. Similar observations were made for the concentration dependence of the shear and extensional viscosities for CNTs dispersed in a Newtonian solvent;[46] however, here, the presence of Psf and PS-PAA block polymer in the ink contributed to substantially higher viscosity values and longer pinching times. As using a shear viscosity comparable to the CNT-free ink allows printing with the same flow rate and pump pressure, and the use of a lower particle concentration is processing friendly, the 0.1% CNT-based ink was selected for DIW 3D printing of structured sorbents. In addition to delayed pinch-off that promoted the formation of continuous filaments, CNTs also contributed improvements in mechanical properties, which is advantageous for maintaining sorbent structure under operating pressures.[47–50]

Please cite this article in press as: Xu et al., Heavy metal removal using structured sorbents 3D printed from carbon nanotube-enriched polymer solutions, Matter (2022), https://doi.org/10.1016/j.matt.2022.07.012

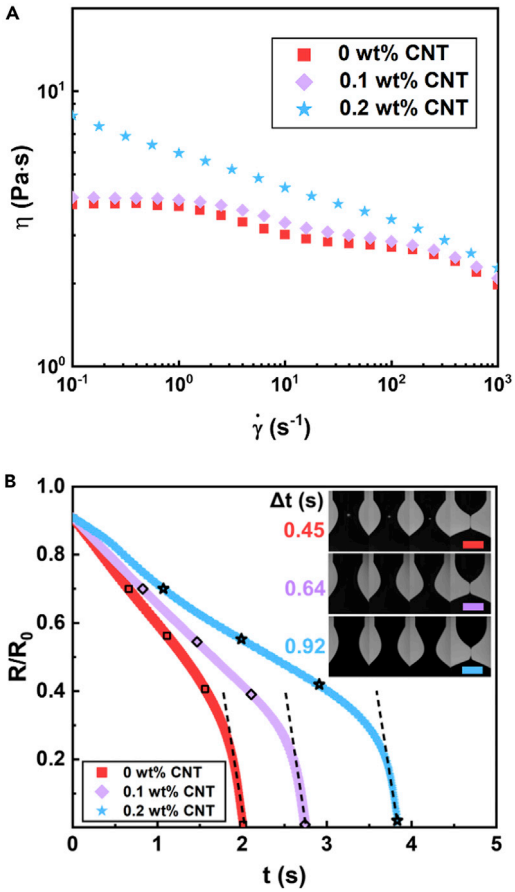

Figure 2. Rheological characterization of the polymer composite inks

The composition of the composite inks is reported in terms of weight loading. All of the inks contained 10% Psf and 2% PS-PAA dissolved in 2P along with varying amounts of CNTs. The red squares, purple diamonds, and blue stars represent the data for inks containing 0%, 0.1%, and 0.2% CNTs, respectively.

(A) Shear viscosity as a function of shear rate for the 3 composite inks.

(B) Dripping-onto-substrate (DoS) rheometry was used to visualize and analyze the radius evolution of pinching necks of the 3 inks. The neck radius evolution data are shown on a linear-linear plot. The inset includes 4 image sequences highlighting the evolution of the neck shape over time. Scale bars, 1 mm. Each montage begins with a snapshot at $R/R_0 = 0.7$ (time t_0) and ends with the filament right before pinch-off (time t_f). The middle 2 panels are taken at time Δt and $2\Delta t$, where $\Delta t = (t_f - t_0)/3$. The time step, Δt equals 450, 640, and 920 ms for the 0%, 0.1%, and 0.2% CNT inks, respectively. The snapshots correspond to the points highlighted in each radius evolution plot.

Controlled humidity environment creates hierarchically structured sorbents

After establishing the ink composition, the relative humidity of the vapor environment was optimized for the successful fabrication of sorbents. Upon exposure to the humid environment, water vapor penetrates into the extruded ink. As water vapor penetrates into the filament, the concentration of water increases and initiates liquid-liquid demixing and gelation/solidification of the ink. At low humidity (e.g., relative humidity [RH] 35%), the rate of intrusion of water vapor was too slow to initiate gelation on the timescale of filament extrusion. As a result, a puddle of ink formed on the surface of the printing platform. However, when the humidity was high (e.g., RH 80%), the extruded filaments phase separated quickly such that they solidified on the surface before the next layer was deposited. As a result, delamination was observed after immersing the membranes in the nonsolvent bath. Examples of these failures are shown in Figure S2.

Please cite this article in press as: Xu et al., Heavy metal removal using structured sorbents 3D printed from carbon nanotube-enriched polymer solutions, Matter (2022), https://doi.org/10.1016/j.matt.2022.07.012

For the composite ink formulation used here, the printing process was best executed in a chamber at 50% RH. These conditions balanced the considerations needed to control the molecular through macroscale features of the sorbents. Ideally, gelation and phase separation of the ink would begin as it is being extruded such that a gel-like skin forms around the filaments. In this way, the deposited solution cannot flow to the nearby area and the printed structure retains its shape on the substrate. Within the optimal humidity range, while enough water vapor penetrates into the filaments to form a gel, not enough is imbibed to fully solidify the outer surface. As a result, the deposited filament can adhere to the underlying layer. The rate of nonsolvent intrusion also affects the sorbent nanostructure. Directly plunging the extruded ink into a water bath would initiate rapid liquid-liquid demixing and the formation of finger-like voids across the filament cross-section.[41] Using water vapor to initiate phase separation slows this process and results in a spongy bicontinuous structure with high surface area throughout the filaments.[43]

The SVIPS method allows the PAA blocks to segregate toward the pore walls due to their relative hydrophilicity. After printing concluded, the sorbents were immersed in a water bath to fully exchange the solvent and nonsolvent. Subsequently, annealing the samples in warm water helped to ensure that the PAA brushes line the surface of the sorbents while the Psf forms the matrix of the filaments. In this way, the combination of DIW 3D printing and SVIPS processes can be used to control the sorbent structure across several length scales with micron-scale channels between filaments resulting from the printing process, while the filaments themselves contain nanoscale pores due to phase separation processes. A schematic of the filaments and channel structure is shown in Figure 1B.

The images and micrographs in Figure 3 examine the structural features of the printed sorbents at increasing magnifications. Figure 3A shows the full size of the 2 × 2-cm woodpile structure. Figures 3B and 3C provide closer views of the channels that form between the filaments as well as the filaments themselves, respectively. As designed, the spacing between filaments was ~250 μm. Independent of the channel spacing, the width of the filaments was ~250 μm, which is consistent with the diameter of the dispensing needle. A high-magnification micrograph of the filament nanostructure is provided in Figure 3D. Pores ~300 nm in diameter percolated throughout the filament. Furthermore, the surface of these pores was dotted with nodules ~30 nm in size. Based on their characteristic size as well as the fact that these nodules are not observed when the composite ink does not contain PS-PAA (Figure S3), it is hypothesized that the nodules are the PAA brushes segregated to the surface of the filaments. A few CNTs appear distributed throughout the porosity of the filaments.

Micrographs of the sorbent cross-section are displayed in Figure 4. The final sorbents were thick and relatively rigid, which made obtaining a view of the whole cross-section difficult. Instead, several layers were separated from the sorbent and fractured after freezing in liquid nitrogen. The uniform thickness, ~14 μm, of each layer is highlighted in the lower magnification micrograph (Figure 4A). The high magnification micrograph in Figure 4B focuses on the cross section of a single filament layer and demonstrates the isotropic, spongy structure that results from optimizing the humidity of the printing environment. Additional micrographs of the sorbent structures are provided in Figures S4 and S5.

The structures achieved through the combination of 3D printing and the SVIPS process result in highly permeable sorbents. The volumetric water flux, J_w, is one metric for

Please cite this article in press as: Xu et al., Heavy metal removal using structured sorbents 3D printed from carbon nanotube-enriched polymer solutions, Matter (2022), https://doi.org/10.1016/j.matt.2022.07.012

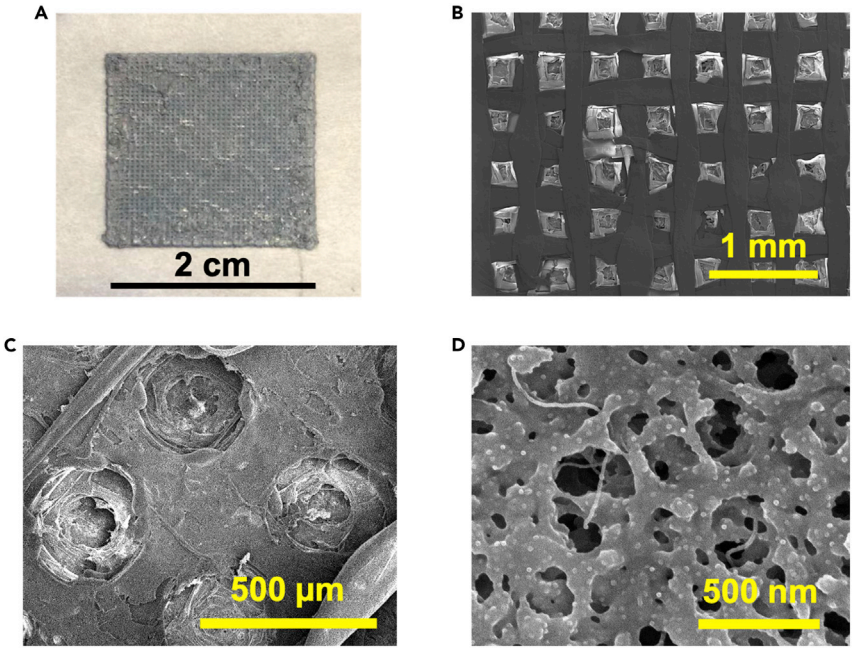

Figure 3. Structural analysis of the sorbent surface

(A) A digital photograph of a 3D-printed PAA-functionalized sorbent on a nonwoven polyester substrate. Scale bar, 2 cm.

(B) A low-magnification scanning electron micrograph of the PAA-functionalized sorbent showing the arrangement of polymer filaments. Scale bar, 1 mm.

(C) A scanning electron micrograph demonstrating the large channel that forms between the crossing filaments of the woodpile structure. Scale bar, 500 μm.

(D) A high-magnification SEM micrograph highlighting the nanostructure of the printed filaments. The CNT are dispersed throughout the material, while the PAA brushes are distributed over the surface of the nanoporous structure. Scale bar, 500 nm.

quantifying sorbent throughput. It can be expressed as the product of the hydraulic permeability, L_p, and the pressure applied to drive flow, ΔP, i.e., $J_w = L_p \times \Delta P$. The blank polyester substrate had a hydraulic permeability of 5.0×10^5 L m^{-2} h^{-1} bar^{-1}, the sorbents with 4 layers of filaments exhibited a permeability of 2.2×10^5 L m^{-2} h^{-1} bar^{-1}, while sorbents with 12 and 24 layers could still achieve high permeability values of 1.7×10^5 and 9.4×10^4 L m^{-2} h^{-1} bar^{-1}, respectively, which is comparable to, or even higher than, commercial microfiltration membranes.[36]

Post-synthetic modifications tailor sorbents for high-affinity metal ion removal

The PAA brushes that segregate to the filament surface provide functional handles to tailor the sorbent chemistry for the high-affinity, high-capacity removal of transition metal ions in water treatment and resource recovery processes (Figure 1B). Branched poly(ethyleneimine) (PEI) was first coupled to the as-printed sorbent using carbodiimide chemistry. The high density of amines within the PEI provides more sites for metal ion capture, as well as the subsequent terpyridine (Terp) coupling reaction. Due to its high affinity for transition metal ions, terpyridine was covalently bound to the PEI-functionalized sorbent using a second carbodiimide coupling reaction to create sorbents that can efficiently capture metal ions at sub-parts per million concentrations. The surface chemistry of the sorbent was monitored after both chemical reactions using attenuated total reflectance-Fourier transform infrared (ATR-FTIR) spectroscopy. The broad peak centered ~3,300 cm^{-1} that appears in

Please cite this article in press as: Xu et al., Heavy metal removal using structured sorbents 3D printed from carbon nanotube-enriched polymer solutions, Matter (2022), https://doi.org/10.1016/j.matt.2022.07.012

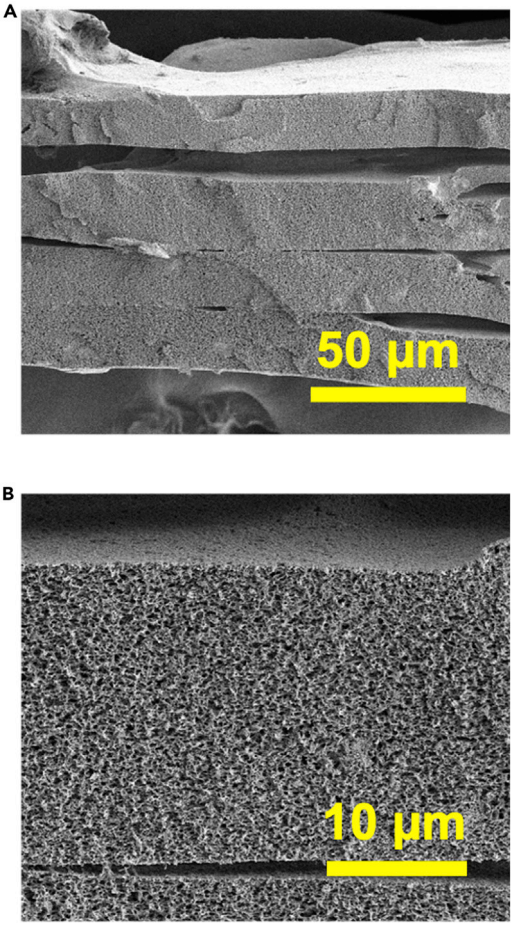

Figure 4. Scanning electron microscopy analysis of the sorbent cross-section

(A) Several layers of printed filaments are shown in cross-section to demonstrate the uniform thickness of the printed layers. Scale bar, 50 μm.

(B) A higher magnification cross-section displays the high surface area porosity of the spongy structure produced by the SVIPS process. Scale bar, 10 μm.

the spectrum for the PEI-functionalized sorbent, but is absent for the PAA-functionalized material (Figure S6), is consistent with the amine bond introduced after the first coupling reaction. As shown in Figure 5A, the new peaks that appear at 1,445 cm^{-1}, 1,563 cm^{-1}, and 1,647 cm^{-1} in the spectrum for the Terp-functionalized sorbent are associated with pyridine groups that are introduced using the second coupling reaction.

The results of static copper (Cu)-binding experiments are consistent with the changes in chemistry observed using FTIR spectroscopy. For example, the impact of the modification protocols and printing parameters on the saturation capacity of the structured sorbents is shown in Figure 5B. Samples with differing numbers of layers and pore wall chemistries were immersed in 100 mM $CuCl_2$ solutions to ensure saturation of the sorbents. Subsequently, the bound Cu ions were released and quantified. The PAA-based sorbents bind Cu primarily through electrostatic interactions and chemical complexation;[51,52] however, even the 24-layer membranes had a relatively low capacity at ~3.2 mmol m^{-2}. The PEI reaction introduced amine groups to provide more binding sites for Cu through chemical chelation and increased the binding capacity more than twice compared to PAA sorbents;[53] the Cu binding capacity for

Please cite this article in press as: Xu et al., Heavy metal removal using structured sorbents 3D printed from carbon nanotube-enriched polymer solutions, Matter (2022), https://doi.org/10.1016/j.matt.2022.07.012

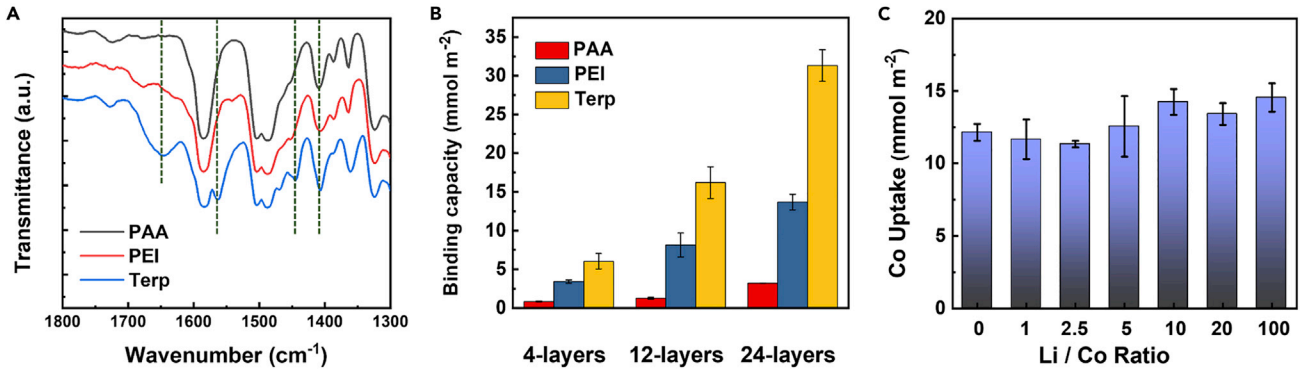

Figure 5. Characterization of the sorbent chemistry and metal ion binding properties

(A) FTIR spectra of the PAA-functionalized, PEI-functionalized, and Terp-functionalized materials over the range of 1,300 $cm^{-1} \leq \tilde{\nu} \leq 1800\ cm^{-1}$. The signals at 1,647 cm^{-1}, 1,563 cm^{-1}, 1,445 cm^{-1}, and 1,410 cm^{-1}, labeled with dashed lines, are consistent with pyridine groups that are introduced through the sequential carbodiimide coupling reactions.

(B) Copper-ion (Cu^{2+}) saturation capacity for sorbents printed with differing number of layers and functionalized with varied metal ion binding groups. Then, 1-cm^2 sections of the sorbents were immersed in 15 mL of a 100-mM $CuCl_2$ solution for 8 h to allow the samples to equilibrated with the solution and reach their maximum binding capacities. Subsequently, the Cu was released for quantification, and the sorbents were regenerated for further use. For the PAA-functionalized and PEI-functionalized materials, an aqueous pH 1.5 HCl solution was used to release the Cu; and for the Terp-functionalized samples, 2 mL of a 50-mM EDTA solution was used to remove the Cu bound on the sorbent surface. The Cu concentration in both retentate and released solutions were measured by ICP-OES to ensure Cu release and closed mass balances. Data points indicate the mean and the error bars represent 1 standard deviation calculated from 3 independent replicate experiments on 3 sorbent samples.

(C) Selective cobalt (Co^{2+}) uptake form mixtures of LiCl and $CoCl_2$; 1-cm^2 sections of the 24-layer Terp-functionalized sorbent were immersed in 5 mL of each solution. The Co^{2+} concentration in each solution was held constant at 1 mM, while the Li^+ concentration ranged from 0 to 100 mM. After 8 h in solution, the sorbent was removed, rinsed, and immersed in 5 mL of an aqueous 50-mM EDTA solution to recover the bound Co^{2+}. The Co^{2+} concentration in both the retentate and release solutions was measured by ICP-OES. The reported Co^{2+} uptake was calculated based on the concentration differences between initial and retentate solutions. Data points indicate the mean and the error bars represent 1 standard deviation calculated from 3 independent replicate experiments on 3 sorbent samples.

24-layer PEI sorbents was 13.7 mmol m^{-2}. After the Terp coupling reaction, the sorbents had higher affinity toward Cu and could form more stable complexes,[54–56] which increased the saturation capacity to 31.3 mmol m^{-2} for the 24-layer Terp-functionalized sorbents. The mass of each layer was ~0.21 mg; thus, the saturation capacity of a layer of the Terp-functionalized material was ~0.65 mmol g^{-1}, which is comparable to membrane sorbents based on this chemistry.[43] Notably, saturation capacity increased linearly with the number of layers, which indicates that adsorption was achieved throughout the whole sorbent structure independent of thickness and chemistry.

Cu removal experiments were also executed by immersing the 1-cm^2 samples in 5 mL of 1 mM $CuCl_2$ followed by releasing the bound Cu ions (Figure S7). As expected, membranes with higher binding capacities removed a higher percentage of the dissolved ions. Notably, the high capacity of the 24-layer Terp-functionalized sorbents, which weighed only ~5 mg, allowed ~50% removal. The blue color of the sorbent after this experiment can be seen in Figure S8. Critically, no significant changes in the amount of Cu bound or removed were observed as sorbents were regenerated and reused during this series of experiments, which indicated the stable covalent attachment of the binding ligands, as well as the robust performance of the sorbents upon recycling.

The high affinity of the Terp ligand toward transition metal ions provides several potential applications for these sorbents. For example, methods are needed to recover and recycle critical materials from non-traditional sources, electronics waste, and spent batteries.[57] In this regard, the separation of cobalt (Co) and lithium (Li) is of

increasing importance.[58] Therefore, the selective recovery of Co^{2+} from Li^+/Co^{2+} mixtures was investigated by mixing 1 mM $CoCl_2$ with LiCl at molar ratios of Li^+:Co^{2+} that ranged from 0 to 100. Then, 1-cm^2 sections of the 24-layer Terp-functionalized sorbent were placed in 5 mL of these mixed solutions. After 24 h, the sorbent was extracted and the amount of Co^{2+} removed was calculated (Figure 5C). Despite the increasing Li concentration, the sorbents achieved a consistent Co^{2+} removal capacity of 12 mmol m^{-2}, which was almost three times higher than PAA-functionalized membranes (Figure S9). Interestingly, for both chemistries, the sorbents exhibited higher Co^{2+} removal capacities when the Li^+ concentration was increased above 10 mM. Critically, the Terp-functionalized sorbent retained a significant fraction of its capacity (7.5 mmol m^{-2}) and selectivity toward Co when the pH of the 100:1 Li^+:Co^{2+} solution was reduced to pH 1, which is typical of the acidic solutions used to leach critical materials from electronics waste (Figure S10). The reduced Co^{2+} capacity may be attributed to incomplete conversion of the PAA and PEI groups to Terp. These unreacted carboxylate and amine groups can bind Co^{2+} at pH 5.5. However, at pH 1, the carboxylic acids are protonated and protons have a higher affinity for the amines. Both of these phenomena reduce the ability of these groups to capture Co^{2+}. After absorption experiments, the samples were regenerated and could be reused several times without losing binding capacity.

The selective recovery of Cu from aqueous salt solutions containing competing divalent or trivalent cations was also examined. From an aqueous mixture of 1 mM $CuCl_2$ and 10 mM $MgCl_2$ at pH 4.4, the binding capacity for Cu^{2+} and Mg^{2+} was 21.8 mmol m^{-2} and 5.8 mmol m^{-2}, respectively. The sum of these two values, 27.6 mmol m^{-2}, is comparable to the original Cu^{2+} binding capacity, 31.3 mmol m^{-2}, determined using an aqueous solution of 100 mM $CuCl_2$. The carboxylic acid groups that remain after the sorbent functionalization process can bind Mg^{2+} through electrostatic interactions, thereby reducing the amount of Cu^{2+} captured while maintaining the total capacity toward divalent cations. In addition, the binding capacity for Cu^{2+} and Al^{3+} from an aqueous mixture of 1 mM $CuCl_2$ and 10 mM $Al(NO_3)_3$ at pH 3.9 is 15 mmol m^{-2} and 0 mmol m^{-2}, respectively. The reduced Cu^{2+} capacity and immeasurable Al^{3+} binding capacity may be attributed to the PAA repeat units being protonated and the PEI groups having a higher affinity for protons at pH 3.9. These results are reported in Figure S11.

Throughout the series of absorption experiments, the samples were regenerated and could be reused without losing binding capacity. Specifically, in the series of experiments examining Cu^{2+} removal and the selective binding of Co^{2+} from mixtures of Co^{2+}/Li^+, each sample reported in the paper was used for at least 3 cycles of Cu^{2+} removal and 21 cycles of Co^{2+}/Li^+ selectivity experiments. After each of these 24 experiments, the samples were regenerated and reused. No significant reduction in the performance or saturation capacity was observed. In this regard, the sorbents have good stability and reusability.

Structural control enables metal ion removal under dynamic flow conditions

While the batch adsorption experiments demonstrate the high affinity and capacity of the 3D-printed sorbents for metal ion capture under static conditions, adsorptive separations are dynamic processes. Therefore, flowthrough experiments were carried out using the apparatus shown in Figure S12 to characterize performance under flow conditions. A sorbent sample was fixed in a filter holder connected to a syringe pump that contained 100 mL of a 1-ppm $CuCl_2$ solution (472 ppb Cu^{2+} solution). Once initiated, the syringe pump drove the flow of solution through the sorbent at a constant flow rate of 0.092 or 0.35 mL min^{-1}, and the permeate solution was

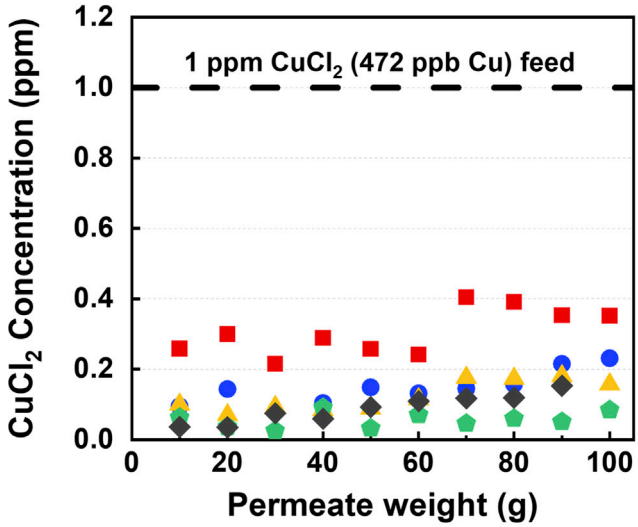

	Symbol	Gz	Flux (L m^{-2} h^{-1})	Layers	Channel width (μm)
i	■	24	300	48	250
ii	●	6.3	78.8	48	250
iii	▲	6.3	300	48	250
iv	⬟	4.0	300	72	mix
v	◆	1.6	78.8	48	125

Figure 6. Flowthrough experiments characterize the dynamic capture of Cu^{2+} from a 1-ppm $CuCl_2$ solution

The 0.7-cm^2 sections of Terp-functionalized sorbents were used in these experiments. Samples of the effluent were collected in 10-g aliquots and analyzed using ICP-OES. The concentration of Cu^{2+} in the effluent is plotted as a function of cumulative mass of treated solution. Each experiment represents operation at a different Graetz number (Gz). (i) Gz = 24 resulted from using a single 48-layer sorbent with 250-μm-wide channels and a constant flux of 300 L m^{-2} h^{-1}. (ii) Gz = 6.3 conditions were realized using a single 48-layer sorbent with 250-μm-wide channels and the flux of 78.8 L m^{-2} h^{-1}. (iii) A Gz = 6.3 was also produced by using two 24-layer sorbents with 250-μm-wide channels stacked in series, and operating at the flux of 78.8 L m^{-2} h^{-1}. (iv) Gz = 4.0 was generated by stacking two 24-layer sorbents with 250-μm-wide channels and one 24-layer sorbent with 125-μm-wide channels in series and operating at the flux of 300 L m^{-2} h^{-1}. (v) A Gz = 1.6 resulted from stacking two 24-layer sorbents with 125-μm-wide channels in series, and operating at 78.8 L m^{-2} h^{-1}.

collected in 10-g aliquots. Because the sorbent had an area of 0.7 cm^2, these flow rates correspond to operating at a constant flux of 78.8 or 300 L m^{-2} h^{-1}. The concentration of Cu^{2+} in the permeate solutions is plotted versus the cumulative mass of permeate in Figure 6.

The Graetz number (Gz), which compares the rate of convective flow through the sorbent to the rate of solute diffusion to binding sites, was used to guide the structural design of the sorbents. The Gz is calculated using Equation 1.

$$Gz = \frac{d^2 \, v}{l \, D} \qquad \text{(Equation 1)}$$

Here, d is the channel width; v is the average velocity of the mobile solution in the channel; l is the sorbent thickness; and D is the diffusion coefficient of the solute. The sorbent thickness, l, is determined using the product of the number of

Please cite this article in press as: Xu et al., Heavy metal removal using structured sorbents 3D printed from carbon nanotube-enriched polymer solutions, Matter (2022), https://doi.org/10.1016/j.matt.2022.07.012

deposited layers and the individual layer thickness based on the SEM micrographs (14 μm). The diffusion coefficient of $CuCl_2$ in water is 1.3×10^{-5} cm^2 s^{-1}.[59] The channel width was controlled during printing and validated from SEM micrographs. The average velocity of fluid within the channel is equal to the volumetric flux divided by the areal fraction of the channels (~25%); thus, the average velocity in the channel is four times higher than J_w. Therefore, for example, a 48-layer sorbent, l = 672 μm, with 250-μm-wide channels operating at 300 L m^{-2} h^{-1} (v = 333 μm s^{-1}) yields Gz = 24.

The 48-layer sorbent operating at a high flow rate had the largest Gz and lowest adsorption of Cu^{2+}, removing ~70% of the Cu ions from 100 mL of the feed solution. From this baseline case, the Gz was reduced by increasing the sorbent thickness, reducing the flow rate through the sorbent, and decreasing the channel width. For example, using the same 48-layer sorbent or stacking two 24-layer sorbents in series and operating at a lower flux of 78.8 L m^{-2} h^{-1} created Gz = 6.3 conditions. Both systems had much lower Cu concentration in the effluent permeate, suggesting that the longer residence time gave the Cu ions more time to diffuse to the binding sites. In turn, more Cu could be absorbed. Stacking two membranes with 125-μm-wide channels and operating at 78.8 L m^{-2} h^{-1}, decreased the Gz number to 1.6. The diffusion time from the center of the channel to the filament surface was reduced to 25% of the time needed for the 250-μm-wide channels, resulting in more than 95% of the Cu being removed. Placing two sorbents with 250-μm-wide channels and one with 125-μm-wide channels together in series achieved similar Cu^{2+} removal performance but while operating at a higher flux of 300 L m^{-2} h^{-1} (Gz = 4.0), which supported the possibility of using the membranes at a short timescale, and suggested the importance of designing hierarchical, patterned structures to enable the efficient capture of target solutes from flowing solutions.

Based on prior measurements,[43] the metal ion binding kinetics were assumed to be instantaneous. Therefore, in this context, smaller Gz number conditions enhanced the diffusion and improved removal performances, which indicated that the diffusion-limited mass transfer existed during the flowthrough tests.[60] Moreover, the slightly increasing trend in concentration when collecting more permeate suggested that the resistance of ion transport inside the pores may present a further barrier. Cu could occupy the binding sites located near the channels easily, hindering further diffusion into the nanoscale pore structure, thereby increasing concentration for the last 40 g of permeate. Thus, work to achieve sufficient ion diffusion in both channels and nanoscale pores is an important future design goal.

Printing thicker sorbents represents one method for enhancing the performance of the structured sorbents reported here. Importantly, this strategy needs to be implemented while maintaining reasonable operating pressures. The operational pressure can be estimated by recalling that $J_w = L_p \times \Delta P$. Moreover, because L_p is inversely proportional to sorbent thickness, the hydraulic permeability of a 48-layer sorbent is assumed to be equal to 4.7×10^4 L m^{-2} h^{-1} bar^{-1} (i.e., half the value reported for the 24-layer sorbent). Therefore, for condition i of the flowthrough experiments reported in Figure 6, the operational pressure drop was only 6.3×10^{-3} bar (0.09 psi). A typical operating pressure for microfiltration membranes is 9 psi. At this pressure, a 4,800-layer, 6.7-cm-thick sorbent would be able to maintain a flux of 300 L m^{-2} h^{-1} while reducing the Gz 100-fold relative to condition i.

The flexibility associated with the combination of DIW 3D printing and a SVIPS process provides several opportunities to tailor the properties of sorbents for enhanced

performance in target applications. For example, in addition to reducing the Gr by increasing the thickness of the sorbent, DIW 3D printing provides spatial control of the lattice geometries, thereby affording the possibility of tailoring the flow channels to enhance mass transfer rates without reducing permeability. Specifically, making the flow channels more tortuous to increase residence times[61] or to induce secondary flows[33] can result in more efficient solute capture profiles. Alternatively, the sorbents reported here have comparable saturation capacities but higher permeabilities than membrane-based sorbents developed from similar material chemistries. Because permeability is determined by the micron-scale structures formed during DIW 3D printing, it should be possible to achieve even higher capacities, while maintaining a high permeability through careful design of the polymer composite inks. For example, sorbents based on self-assembled materials exhibited Cu^{2+} binding capacities that were ~7× higher than those reported here.[62] Going forward, these materials could be incorporated in CNT-enriched solutions that exhibit the rheological characteristics (e.g., increased extensional viscosity and pinching times) needed to 3D print them as structured sorbents. Finally, while the terpyridine moiety used here enabled the efficient capture of transitions metals, numerous other contaminants and resources need to be separated from solution (e.g., per- and polyfluoroalkyl substances,[5] nutrients,[6] biologics[7]). In this regard, the demonstrated ability to manipulate the sorbent chemistry using straightforward coupling reactions suggests the versatility and broad applicability of the platform. Hierarchically structured materials could be readily functionalized with high-affinity ligands, peptides, or enzymes to achieve fit-for-purpose separations.[63] By stacking sorbents in series, it could be possible to realize high-throughput filtrations capable of separating multiple components in a single pass.

Conclusions

In summary, hierarchically structured sorbents were fabricated by combining DIW 3D printing with a SVIPS process. Composite inks were formulated by enriching a polymer solution initially developed for membrane fabrication with CNTs, which led to delayed pinch-off times and enabled the formation of continuous filament structures. The humidity of the printing environment was tailored to initiate the SVIPS process as these filaments were being deposited such that highly permeable sorbents with well-formed channels and tightly arranged layers could be produced. In addition, the SVIPS process generated nanostructured porosity within the filaments that imbued the sorbents with high capacities for solute capture. Introducing selective functional groups through the PAA brushes that lined the nanoporous surface of the filaments increased the binding affinity toward transition metal ions. This affinity was demonstrated by the selective recovery of Co^{2+} from mixtures containing Co and Li dissolved at pH 1 while the rapid mass transfer of the sorbents was evidenced by the efficient removal of Cu^{2+} during dynamic flowthrough experiments. Furthermore, the sorbents could be easily regenerated and reused by releasing bound ions. The methodology described in this work provides a promising approach for using 3D printing technology for the fabrication of functional polymer sorbents that overcome the capacity-permeability trade-off and allow for the targeted recovery of dilute solutes.

EXPERIMENTAL PROCEDURES

Resource availability

Lead contact

Further information and requests for resources and reagents should be directed to and will be fulfilled by the lead contact, William A. Phillip (wphillip@nd.edu).

Please cite this article in press as: Xu et al., Heavy metal removal using structured sorbents 3D printed from carbon nanotube-enriched polymer solutions, Matter (2022), https://doi.org/10.1016/j.matt.2022.07.012

Materials availability

This study did not generate new, unique reagents.

Data and code availability

Data required to evaluate the conclusions of this article are provided within the article and supplemental information. Raw data will be made available from the lead contact upon reasonable request.

Codes for printing the woodpile pattern were generated by the Aerotech A3200 Motion Composer and the movement of the all of the axes were controlled by the Aerotech A3200 CNC Operator. MATLAB codes were used to analyze DoS videos, and can be made available from the lead contact upon reasonable request.

Materials

Multi-walled CNTs (>98%, outer diameter × length 6–13 nm × 2.5–20 μm), Psf (M_n = 22 kg mol^{-1}), 2-pyrrolidinone (2P, 99%), PEI (M_n = 60 kg mol^{-1}, 50 wt % in water), ethylenediaminetetraacetic acid (EDTA), sodium hydroxide (NaOH, ≥97%), potassium hydroxide (KOH, ≥85%), hydrochloric acid (HCl, 37%), nitric acid (HNO_3, 70%), Co(II) chloride ($CoCl_2$, 97%), Cu (II) chloride ($CuCl_2$, 97%), magnesium chloride ($MgCl_2$, ≥98%), aluminum nitrate nonahydrate ($Al(NO_3)_3$, ≥99%), sodium bicarbonate ($NaHCO_3$), 1-hydroxybenzotriazole hydrate (HOBt, 98%), and ethanol (EtOH) were purchased from Sigma-Aldrich. Also, ε-caprolactone (99%) was purchased from Alfa Aesar. Dimethylsulfoxide (DMSO, 99%) was obtained from Beantown Chemical. 4′-Chloro-2,2′:6′,2″-terpyridine (97%) was purchased from AMBeed. Tetrahydrofuran (THF) was purchased from Macron Fine Chemicals. 1-Ethyl-3-(3-dimethylaminopropyl) carbodiimide hydrochloride (EDC·HCl, 99.9%) was obtained from Chem-Impex Int'l. PS-PAA (M_n: 70.5-*b*-13.0 kg mol^{-1}, $Đ$ = 1.10) was purchased from Polymer Source. Nonwoven polyester substrates (Cranemat CU632(UF), 100% polyester) were provided by Neenah Filtration. Unless noted otherwise, all of the materials were used as received. Deionized (DI) water was provided by a Millipore water purification system (Milli Q Advantage A10).

6-(2, 2′: 6′, 2″-Terpyridin-4′-yloxy) hexanoic acid (Terp-COOH) synthesis

The Terp-COOH synthesis followed a previously published reaction scheme and protocols.[43,64] In summary, powdered KOH (1.85 g) was added to DMSO (10 mL) at 65°C; then, ε-caprolactone (1.49 g, 13.07 mmol) was added dropwise to the solution while stirring. After adding all of the ε-caprolactone, the solution was left to react at 65°C for 30 min; then, 4′-chloro-2,2′:6′,2″-terpyridine (1.74 g, 6.49 mmol) was added to the reaction vessel. The reaction mixture was stirred at 65°C for 48 h, then allowed to cool to room temperature. Subsequently, 400 mL of DI water was added to the mixture, followed by the dropwise addition of 1M HCl until a precipitate formed. This crude product was isolated by filtering with a Buchner funnel. The final product was purified by recrystallization in THF and dried in vacuum. Synthetic scheme and ^{1}H-nuclear magnetic resonance (^{1}H-NMR) spectra are shown in Figure S13.

Sorbent fabrication

Ink preparation

The polymer composite ink was prepared by dissolving 10% (by weight) Psf and 0.1% (by weight) CNTs in 2P at 80°C under continuous stirring. Then, 2% (by weight) PS-PAA block polymer was added to the mixture, which was stirred at 60°C until a homogenous solution was obtained. The solution was allowed to sit at room temperature to degas for 1 day. Immediately before printing, the solution was sonicated to disperse the CNTs in the ink.

Sorbent printing in humid chamber

Structured sorbents were printed in a humidity chamber that had an RH controlled between 35% and 85%. A humidity controller (Inkbird IHC200) and humidifier (Vicks V745) were used to keep the humidity in the desired range. The polymer composite ink was extruded from a 3-mL BD syringe using a 1.5-in.-long, 25-G dispensing needle (BSTEAN, inner diameter 0.26 mm). A syringe pump (Harvard Apparatus Pump 11 Elite) operating at 50% force level controlled the flow rate of ink through the needle at a constant value of 0.04 mL min^{-1}. The x-y planar (Aerotech) and z-axis controller (home-designed and made by Aerotech) were connected to a computer by amplifiers (NDRIVE ML10-40-IO-MXH for x and y axes, NdriveMP10 for z-axis). Patterns were designed using an Aerotech A3200 Motion Composer and the movement of all of the axes were controlled by an Aerotech A3200 CNC Operator. During printing, the x-y planar moved at a velocity of 50 mm s^{-1}. Initially, the needle was positioned at the bottom left corner of the woodpile structure. From this position, the planar was moved down for 20 mm, then left for 0.5 mm, and up for 20 mm to form two parallel filaments with a 500-μm gap between them. This movement pattern was repeated for 40 cycles to create a single layer. From its final position at the top right corner of the designed pattern, the z-axis controller moved the needle up 10 μm vertically and the x-y planar moved right to left to deposit the next layer of the structure, with filaments perpendicular to the prior layer. At the end of depositing this layer, the needle was again situated above the bottom left corner of the structure and the process could be repeated.

Sorbent annealing

After the printing routine was complete, the sorbent was exposed to the humid environment for 5 min before being immersed in the nonsolvent (DI water) bath, where it remained overnight (~12 h) to allow for solvent exchange. The printed sorbent was annealed in a DI water bath at 80°C for 6 h to facilitate the segregation of the PAA blocks to the pore walls. The sorbents were then stored in DI water until further functionalization.

Sorbent functionalization

The surface chemistry of the as-printed PAA-functionalized sorbents was modified using sequential carbodiimide coupling reactions.[43] First, branched PEI was incorporated to increase the sorbent-binding capacity. The reaction was carried out using a solution containing 5 mM PEI, 50 mM EDC·HCl, 250 mM HOBt, and 100 mM $NaHCO_3$. The solution was stirred until it was well mixed. The pH of this reactive PEI solution was adjusted by adding 1 M HCl until the solution was at pH 6, as determined by pH test strips (VWR). PAA-functionalized sorbents were then immersed in the solution at room temperature without stirring for 5 days. After rinsing them thoroughly with DI water, the PEI-functionalized sorbents were stored in DI water. The terpyridine functionalization proceeded by immersing the PEI-functionalized sorbents in a solution containing 8.5 mM Terp, 10 mM EDC·HCl, and 25mM HOBt dissolved in ethanol. The solution was pre-heated to 70°C under stirring until it was homogenous. Subsequently, the PEI-functionalized sorbents were added to the 70°C solution and left without stirring for 12 h. After the solution cooled to room temperature, the sorbents were rinsed thoroughly with EtOH and DI water and stored in DI water.

Materials characterization

FTIR

The surface chemistries of the sorbents were analyzed using a Bruker Tenor 27 FTIR spectrophotometer operating in ATR mode. Before analysis, sections of the sorbent

Please cite this article in press as: Xu et al., Heavy metal removal using structured sorbents 3D printed from carbon nanotube-enriched polymer solutions, Matter (2022), https://doi.org/10.1016/j.matt.2022.07.012

were dried in a vacuum oven overnight and stored in clean petri dishes. ATR-FTIR spectra were collected using 64 scans over a range of wavenumbers, $\tilde{\nu}$, $600 \leq \tilde{\nu} \leq 4{,}000\ cm^{-1}$.

^{1}H-NMR

^{1}H-NMR spectra for the Terp-COOH were acquired using Bruker AVANCE III HD 500. Samples were prepared by dissolving dried Terp-COOH in deuterated dimethyl sulfoxide (DMSO-d_6) at 10 mg mL^{-1}.

Ink rheology

The steady shear viscosity, $\eta(\dot{\gamma}) \equiv \tau_{12}/\dot{\gamma}$ was characterized using a cone-and-plate geometry (50 mm diameter, 1° cone angle) on an Anton Paar MCR 302 Rheometer (torque range 10^{-5}–200 mN · m). Here, the shear stress, τ_{12}, in response to imposed shear rates in the range of $\dot{\gamma} = 0.01$–$10^3\ s^{-1}$ was measured at constant temperature (maintained using a Peltier element). The pinching dynamics and extensional rheology response were characterized using DoS rheometry. A finite volume of fluid is dispensed at a low and fixed flow rate ($Q = 0.02\ mL\ min^{-1}$) through a stainless-steel nozzle with outer and inner diameters of $D_0 = 2.108$ mm and $D_i = 1.6$ mm, respectively. The shape evolution of the neck of the hourglass-shaped liquid bridge, formed with an aspect ratio of $H/D_0 \approx 3$ on a partially wetting substrate, were visualized using an imaging system that includes a light source, a diffuser, a high-speed camera (Fastcam SA3 with a Nikkor 3.1× zoom [18–25 mm] lens), and an attached macro lens to improve magnification. Reasonably high frame rates (2,000 frames per second) were used, and the DoS videos are analyzed with specially written MATLAB codes to determine the minimum neck radius as a function of time. The experimental setup, design considerations, specific advantages contrasted to other extensional rheology methods, and various approaches to analyzing datasets are detailed in our previous contributions.[44,45,65,66]

Sorbent characterization and testing

Scanning electron microscopy

Selected samples were imaged using an FEI-Magellan 400 field-emission scanning electron microscope or a Thermo Prisma Environmental-scanning electron microscope. Samples for surface analysis were cut from the printed sorbents without further actions. Samples for cross-sectional analysis were prepared by immersing the sorbents in liquid nitrogen until the liquid nitrogen stopped bubbling vigorously (~1 min), followed by freeze fracturing. All of the samples were sputter-coated with 2 nm of iridium to prevent charging. The values 5 keV and 13 pA was chosen to generate the surface scanning electron microscopy micrographs, and 2 keV and 6.3 pA were chosen to generate the cross-section area scanning electron microscopy.

Permeability test

A circular section of sorbent, 1.4 cm in diameter, was assembled into a 10-mL stirred cell (EMD Millipore Amicon 8003), with the surface layer facing the feed reservoir. Due to the high hydraulic permeability of the sorbents, the 10-mL stirred cell would be depleted within a few seconds even at low transmembrane pressures (i.e., <0.1 bar). Therefore, the stirred cell was connected to a homemade 800 mL reservoir that allowed for extended permeability experiments. The stirred cell and reservoir were filled with DI water and a pressure between 0.02 and 0.03 bar was applied to the reservoir. The permeate solution was collected in a container that rested on a balance, and the mass of the collected solution was recorded every 5 s for 3 min. Hydraulic permeabilities were calculated by regressing the water flux and transmembrane pressure data.

Inductively coupled plasma-optically emitting spectrophotometry (ICP-OES)

The concentration of Cu and Co in solution was measured using a Prep3 Optima 8000 inductively coupled plasma-optically emitting spectrophotometer. Samples for ICP-OES analysis were prepared by adding 0.1 mL of the solution containing the metal ion into 5 mL of 3.5% (v/v) nitric acid.

Ion uptake

Batch metal ion adsorption experiments were performed using 1 × 1 cm^2 sections of the sorbents. A schematic of the testing process is shown in Figures S10A and S10B. Sorbent samples were submerged in 5 mL of a 1-mM $CuCl_2$ or 15 mL of a 100-mM $CuCl_2$ solution for 8 h. They were subsequently extracted and rinsed with excess DI water to remove free and loosely bound ions. To completely release the bound Cu ions from the PAA-functionalized and PEI-functionalized samples, the sorbent was immersed in 2 mL of an aqueous HCl solution (pH = 1.5) for 8 h. Following the binding experiments, metal ions were removed from the terpyridine-functionalized materials by immersing the sorbents in 2 mL of a 50-mM EDTA solution. The pH of the EDTA solution was adjusted to neutral pH by adding NaOH. The metal ion concentration in the retentate (i.e., treated) and released solutions were analyzed via ICP-OES. After release of the metal ions and before an experiment, the sorbents were regenerated for reuse by immersing the samples in 10 mL pH 12 NaOH solution for 8 h and then rinsing them with an excess amount of DI water.

For Co adsorption experiments, 1 × 1 cm^2 sections of 24-layer Terp-functionalized sorbent was immersed in 5 mL of a solution containing dissolved Co and Li salts. The solution had a constant $CoCl_2$ concentration of 1 mM and varied LiCl concentrations ranging between 0 and 100 mM. The sorbent was allowed to soak in this solution for 8 h, then was rinsed with excess DI water to remove free and loosely bound ions. The bound ions were completely released by immersing the sorbent in 5 mL 50 mM EDTA solution for 8 h. The Co concentration in the retentate (i.e., treated) and released solutions were analyzed via ICP-OES. After release of the metal ions and before an experiment, the sorbents were regenerated for reuse by immersing the samples in 10 mL pH 12 NaOH solution for 8 h and then rinsing them with an excess amount of DI water.

Ion uptake was calculated by Equation 2:

$$Q = \frac{C_R \times V}{A} \quad \text{(Equation 2)}$$

Here, Q is the ion uptake, C_R is the ion concentration in the released solution, V is the volume of released solution, and A is the area of the membrane. Three membrane pieces made in three different batches were used to repeat all of the experiments. Critically, no significant changes in the amount of Cu bound or removed were observed during this series of experiments, which indicated the stable covalent attachment of the binding ligands as well as the good recycling and reuse performance of the sorbents.

Flowthrough test

A schematic of the flowthrough capture experiments used to characterize the Terp-functionalized sorbents is shown in Figure S10C. Sections of the sorbent 1 cm in diameter were cut from the printed samples and packed into a 0.7-cm^2 filter (Sterlitech Swinnex 520100), with the printed surface facing the feed solution. The 1-ppm $CuCl_2$ solution was loaded into a 100-mL syringe (Wilburn Medical USA) that was connected to the filter holder through a Luer lock fitting. A pump (Harvard Apparatus 975 Compact Mechanical Multiple-Syringe Infusion Pump) was used to deliver the feed solution at a constant flow

rate (0.35 mL min^{-1} or 0.092 mL min^{-1}). The solution that permeated through the sorbent was collected in scintillation vials using a homemade apparatus. The apparatus rested on an electronic balance, and its mass was recorded every 5 s. Ten vials were placed around the outside of a circular rotating disk, which was controlled by a MATLAB-programmed motor, after collecting every desired amount of solution (i.e., 10 g), the motor automatically rotated, and a new vial was placed under the filter to collect the next 10 g of permeate solution. The ion concentrations in permeate solutions were analyzed via ICP-OES. Membranes were regenerated using the same protocols that were used in the batch uptake experiments.

SUPPLEMENTAL INFORMATION

Supplemental information can be found online at https://doi.org/10.1016/j.matt.2022.07.012.

ACKNOWLEDGMENTS

This work was kindly supported by the National Science Foundation (NSF) through awards 1924715 (University of Notre Dame) and 1924714 (Purdue University), and we appreciatively acknowledge this support. We would like to thank the Center for Environmental Science and Technology at the University of Notre Dame (CEST) and the Notre Dame Integrated Imaging Facility (NDIIF). Portions of this research were performed with instruments at these facilities. T.K. gratefully acknowledges support for this project from the Vincent P. Slatt Fellowship for Undergraduate Research in Energy Systems and Processes, administered by the Center for Sustainable Energy at Notre Dame.

AUTHOR CONTRIBUTIONS

Conceptualization, J.X., V.S., and W.A.P.; methodology, J.X., C.S., V.S., and W.A.P.; investigation, J.X. and C.S.; formal analysis, J.X., C.S., and A.S.B.; writing – original draft, J.X. and C.S.; writing – review & editing, J.X., B.W.B., M.J.W., V.S., and W.A.P.; software, K.G.A. and T.K.; visualization, J.X., C.S., K.G.A., and T.K.; resources, A.S.B.; funding acquisition, B.W.B. and W.A.P.; supervision, B.W.B., M.J.W., V.S., and W.A.P.

DECLARATION OF INTERESTS

The authors declare no competing interests.

Received: March 22, 2022
Revised: May 31, 2022
Accepted: July 11, 2022
Published: August 1, 2022

REFERENCES

1. Sholl, D.S., and Lively, R.P. (2016). Seven chemical separations to change the world. Nature *532*, 435–437. https://doi.org/10.1038/532435a.

2. Kawka, K., Wilton, A.N., Madadkar, P., Medina, M.F.C., Lichty, B.D., Ghosh, R., and Latulippe, D.R. (2021). Integrated development of enzymatic DNA digestion and membrane chromatography processes for the purification of therapeutic adenoviruses. Sep. Purif. Technol. *254*, 117503. https://doi.org/10.1016/j.seppur.2020.117503.

3. Das, S., Wang, Z., Brown, S., Janke, C.J., Mayes, R.T., Gill, G.A., and Dai, S. (2021). Strategies toward the synthesis of advanced functional sorbent performance for uranium uptake from seawater. Ind. Eng. Chem. Res. *60*, 15037–15044. https://doi.org/10.1021/acs.iecr.1c02920.

4. Yuan, Y., Zhao, S., Wen, J., Wang, D., Guo, X., Xu, L., Wang, X., Wang, N., Yuan, Y., Zhao, S., et al. (2019). Rational design of porous nanofiber adsorbent by blow-spinning with ultrahigh uranium recovery capacity from seawater. Adv. Funct. Mater. *29*, 1805380. https://doi.org/10.1002/adfm.201805380.

5. Ateia, M., Alsbaiee, A., Karanfil, T., and Dichtel, W. (2019). Efficient PFAS removal by amine-functionalized sorbents: critical review of the current literature. Environ. Sci. Technol. Lett. *6*, 688–695. https://doi.org/10.1021/acs.estlett.9b00659.

6. Warsinger, D.M., Chakraborty, S., Tow, E.W., Plumlee, M.H., Bellona, C., Loutatidou, S., Karimi, L., Mikelonis, A.M., Achilli, A., Ghassemi, A., et al. (2016). A review of polymeric membranes and processes for potable water reuse. Prog. Polym. Sci. *81*, 209–237. https://doi.org/10.1016/j.progpolymsci.2018.01.004.

7. Singh, N., and Heldt, C.L. (2022). Challenges in downstream purification of gene therapy viral

vectors. Curr. Opin. Chem. Eng. *35*, 100780. https://doi.org/10.1016/j.coche.2021.100780.

8. Yang, X., Martinson, A.B., Elam, J.W., Shao, L., and Darling, S.B. (2021). Water treatment based on atomically engineered materials: atomic layer deposition and beyond. Matter *4*, 3515–3548. https://doi.org/10.1016/j.matt.2021.09.005.

9. Zhang, Y., Guo, J., Han, G., Bai, Y., Ge, Q., Ma, J., Lau, C.H., and Shao, L. (2021). Molecularly soldered covalent organic frameworks for ultrafast precision sieving. Sci. Adv. *7*, eabe8706. https://doi.org/10.1126/sciadv.abe8706.

10. Nguyen, D.T.T., Guillarme, D., Rudaz, S., and Veuthey, J.L. (2006). Fast analysis in liquid chromatography using small particle size and high pressure. J. Sep. Sci. *29*, 1836–1848. https://doi.org/10.1002/jssc.200600189.

11. Takeda, T., Saito, K., Uezu, K., Furusaki, S., Sugo, T., and Okamoto, J. (1991). Adsorption and elution in hollow-fiber-packed bed for recovery of uranium from seawater. Ind. Eng. Chem. Res. *30*, 185–190. https://doi.org/10.1021/ie00049a027.

12. Ouimet, J.A., Xu, J., Flores-Hansen, C., Phillip, W.A., and Boudouris, B.W. (2022). Design considerations for next-generation polymer sorbents: from polymer chemistry to device configurations. Macromol. Chem. Phys. (published online 2022-04-12). https://doi.org/10.1002/macp.202200032.

13. Przybycien, T.M., Pujar, N.S., and Steele, L.M. (2004). Alternative bioseparation operations: life beyond packed-bed chromatography. Curr. Opin. Biotechnol. *15*, 469–478. https://doi.org/10.1016/j.copbio.2004.08.008.

14. Lu, J., and Wang, H. (2021). Emerging porous framework material-based nanofluidic membranes toward ultimate ion separation. Matter *4*, 2810–2830. https://doi.org/10.1016/j.matt.2021.06.045.

15. Weidman, J.L., Mulvenna, R.A., Boudouris, B.W., and Phillip, W.A. (2017). Nanoporous block polymer thin films functionalized with bio-inspired ligands for the efficient capture of heavy metal ions from water. ACS Appl. Mater. Interfaces *9*, 19152–19160. https://doi.org/10.1021/acsami.7b04603.

16. Mazzeo, J.R., DNeue, U., Kele, M., and Plumb, R.S. (2005). Advancing LC performance with smaller particles and higher pressure. Anal. Chem. *77*, 460-A–467-A. https://doi.org/10.1021/ac053516f.

17. Heinonen, J., Sanlaville, Q., Niskakoski, H., and Sainio, T. (2018). Effect of separation material particle size on pressure drop and process efficiency in continuous chromatographic separation of glucose and fructose. Sep. Purif. Technol. *193*, 317–326. https://doi.org/10.1016/j.seppur.2017.10.049.

18. Suresh, P., and Duval, C.E. (2020). Poly(acid)-Functionalized membranes to sequester uranium from seawater. Ind. Eng. Chem. Res. *59*, 12212–12222. https://doi.org/10.1021/acs.iecr.0c01090.

19. Eugene, E.A., Phillip, W.A., and Dowling, A.W. (2021). Material property targets to enable adsorptive water treatment and resource recovery systems. ACS EST Eng. *1*, 1171–1182. https://doi.org/10.1021/acsestengg.0c00046.

20. Heinz, O., Aghajani, M., Greenberg, A.R., and Ding, Y. (2018). Surface-patterning of polymeric membranes: fabrication and performance. Curr. Opin. Chem. Eng. *20*, 1–12. https://doi.org/10.1016/j.coche.2018.01.008.

21. Wang, H., Mi, X., Li, Y., Zhan, S., Wang, H., Mi, X., Zhan, S., and Li, Y. (2020). 3D graphene-based macrostructures for water treatment. Adv. Mater. *32*, 1806843. https://doi.org/10.1002/adma.201806843.

22. Wang, Z., Cui, F., Pan, Y., Hou, L., Zhang, B., Li, Y., and Zhu, L. (2019). Hierarchically micro-mesoporous β-cyclodextrin polymers used for ultrafast removal of micropollutants from water. Carbohydr. Polym. *213*, 352–360. https://doi.org/10.1016/j.carbpol.2019.03.021.

23. Yang, X.Y., Chen, L.H., Li, Y., Rooke, J.C., Sanchez, C., and Su, B.L. (2017). Hierarchically porous materials: synthesis strategies and structure design. Chem. Soc. Rev. *46*, 481–558. https://doi.org/10.1039/c6cs00829a.

24. Zhang, L., Li, Y., Wang, Y., Ma, S., Ou, J., Shen, Y., Ye, M., and Uyama, H. (2021). Integration of covalent organic frameworks into hydrophilic membrane with hierarchical porous structure for fast adsorption of metal ions. J. Hazard Mater. *407*, 124390. https://doi.org/10.1016/j.jhazmat.2020.124390.

25. Hoffman, J.R., and Phillip, W.A. (2020). 100th anniversary of macromolecular science viewpoint: integrated membrane systems. ACS Macro Lett. *9*, 1267–1279. https://doi.org/10.1021/acsmacrolett.0c00482.

26. Tan, L.J., Zhu, W., Zhou, K., Tan, L.J., Zhu, W., and Zhou, K. (2020). Recent progress on polymer materials for additive manufacturing. Adv. Funct. Mater. *30*, 2003062. https://doi.org/10.1002/adfm.202003062.

27. Qian, X., Ostwal, M., Asatekin, A., Geise, G.M., Smith, Z.P., Phillip, W.A., Lively, R.P., and McCutcheon, J.R. (2022). A critical review and commentary on recent progress of additive manufacturing and its impact on membrane technology. J. Membr. Sci. *645*, 120041. https://doi.org/10.1016/j.memsci.2021.120041.

28. Yeong, W.Y., and Goh, G.D. (2020). 3D printing of carbon fiber composite: the future of composite industry? Matter *2*, 1361–1363. https://doi.org/10.1016/j.matt.2020.05.010.

29. Oh, H.J., Aboian, M.S., Yi, M.Y.J., Maslyn, J.A., Loo, W.S., Jiang, X., Parkinson, D.Y., Wilson, M.W., Moore, T., Yee, C.R., et al. (2019). 3D printed absorber for capturing chemotherapy drugs before they spread through the body. ACS Cent. Sci. *5*, 419–427. https://doi.org/10.1021/acscentsci.8b00700.

30. Honaryar, H., LaNasa, J.A., Lloyd, E.C., Hickey, R.J., and Niroobakhsh, Z. (2021). Fabricating robust constructs with internal phase nanostructures via liquid-in-liquid 3D printing. Macromol. Rapid Commun. *42*, 2100445. https://doi.org/10.1002/marc.202100445.

31. Shi, B., Shang, Y., Zhang, P., Cuadros, A.P., Qu, J., Sun, B., Gu, B., Chou, T.W., and Fu, K.K. (2020). Dynamic capillary-driven additive manufacturing of continuous carbon fiber composite. Matter *2*, 1594–1604. https://doi.org/10.1016/j.matt.2020.04.010.

32. Zhang, F., Ma, Y., Liao, J., Breedveld, V., Lively, R.P., Zhang, F., Ma, Y., Liao, J., Breedveld, V., and Lively, R.P. (2018). Solution-based 3D printing of polymers of intrinsic microporosity. Macromol. Rapid Commun. *39*, 1800274. https://doi.org/10.1002/marc.201800274.

33. Beck, V.A., Ivanovskaya, A.N., Chandrasekaran, S., Forien, J.B., Baker, S.E., Duoss, E.B., and Worsley, M.A. (2021). Inertially enhanced mass transport using 3D-printed porous flow-through electrodes with periodic lattice structures. Proc. Natl. Acad. Sci. USA *118*. e2025562118. https://doi.org/10.1073/pnas.2025562118.

34. Al-Shimmery, A., Mazinani, S., Ji, J., Chew, Y.J., and Mattia, D. (2019). 3D printed composite membranes with enhanced anti-fouling behaviour. J. Membr. Sci. *574*, 76–85. https://doi.org/10.1016/j.memsci.2018.12.058.

35. Guillen, G.R., Pan, Y., Li, M., and Hoek, E.M.V. (2011). Preparation and characterization of membranes formed by nonsolvent induced phase separation: a review. Ind. Eng. Chem. Res. *50*, 3798–3817. https://doi.org/10.1021/ie101928r.

36. Baker, R.W. (2012). Membrane Technology and Applications, Third edition (John Wiley).

37. Wang, D.M., and Lai, J.Y. (2013). Recent advances in preparation and morphology control of polymeric membranes formed by nonsolvent induced phase separation. Curr. Opin. Chem. Eng. *2*, 229–237. https://doi.org/10.1016/j.coche.2013.04.003.

38. Wang, F., Altschuh, P., Ratke, L., Zhang, H., Selzer, M., Nestler, B., Altschuh, P., Zhang, H., Selzer, M., Nestler, B., et al. (2019). Progress report on phase separation in polymer solutions. Adv. Mater. *31*, e1806733. https://doi.org/10.1002/adma.201806733.

39. Wan, C.T.C., Jacquemond, R.R., Chiang, Y.-M., Nijmeijer, K., Brushett, F.R., Forner-Cuenca, A., T-C Wan, C., Chiang, Y., Brushett, F.R., Jacquemond, R.R., et al. (2021). Non-solvent induced phase separation enables designer redox flow battery electrodes. Adv. Mater. *33*, 2006716. https://doi.org/10.1002/adma.202006716.

40. Chae Park, H., Po Kim, Y., Yong Kim, H., and Soo Kang, Y. (1999). Membrane formation by water vapor induced phase inversion. J. Membr. Sci. *156*, 169–178. https://doi.org/10.1016/s0376-7388(98)00359-7.

41. Smolders, C.A., Reuvers, A.J., Boom, R.M., and Wienk, I.M. (1992). Microstructures in phase-inversion membranes. Part 1. Formation of macrovoids. J. Membr. Sci. *73*, 259–275. https://doi.org/10.1016/0376-7388(92)80134-6.

42. Ismail, N., Venault, A., Mikkola, J.P., Bouyer, D., Drioli, E., and Tavajohi Hassan Kiadeh, N. (2020). Investigating the potential of membranes formed by the vapor induced phase separation process. J. Membr. Sci. *597*, 117601. https://doi.org/10.1016/j.memsci.2019.117601.

43. Zhang, Y., Vallin, J.R., Sahoo, J.K., Gao, F., Boudouris, B.W., Webber, M.J., and Phillip, W.A. (2018). High-affinity detection and capture of heavy metal contaminants using

block polymer composite membranes. ACS Cent. Sci. *4*, 1697–1707. https://doi.org/10.1021/acscentsci.8b00690.

44. Martínez Narváez, C.D.V., Dinic, J., Lu, X., Wang, C., Rock, R., Sun, H., and Sharma, V. (2021). Rheology and pinching dynamics of associative polysaccharide solutions. Macromolecules *54*, 6372–6388. https://doi.org/10.1021/acs.macromol.0c02751.

45. Dinic, J., and Sharma, V. (2019). Macromolecular relaxation, strain, and extensibility determine elastocapillary thinning and extensional viscosity of polymer solutions. Proc. Natl. Acad. Sci. USA *116*, 8766–8774. https://doi.org/10.1073/pnas.1820277116.

46. Tsentalovich, D.E., Ma, A.W.K., Lee, J.A., Behabtu, N., Bengio, E.A., Choi, A., Hao, J., Luo, Y., Headrick, R.J., Green, M.J., et al. (2016). Relationship of extensional viscosity and liquid crystalline transition to length distribution in carbon nanotube solutions. Macromolecules *49*, 681–689. https://doi.org/10.1021/acs.macromol.5b02054.

47. Lee, T.H., Lee, M.Y., Lee, H.D., Roh, J.S., Kim, H.W., and Park, H.B. (2017). Highly porous carbon nanotube/polysulfone nanocomposite supports for high-flux polyamide reverse osmosis membranes. J. Membr. Sci. *539*, 441–450. https://doi.org/10.1016/j.memsci.2017.06.027.

48. Vega, J.F., Martínez-Salazar, J., Trujillo, M., Arnal, M.L., Müller, A.J., Bredeau, S., and Dubois, P. (2009). Rheology, processing, tensile properties, and crystallization of polyethylene/carbon nanotube nanocomposites. Macromolecules *42*, 4719–4727. https://doi.org/10.1021/ma900645f.

49. Marcourt, M., Cassagnau, P., Fulchiron, R., Rousseaux, D., Lhost, O., and Karam, S. (2018). High Impact Polystyrene/CNT nanocomposites: application of volume segregation strategy and behavior under extensional deformation. Polymer *157*, 156–165. https://doi.org/10.1016/j.polymer.2018.10.032.

50. Arrigo, R., and Malucelli, G. (2020). Rheological behavior of polymer/carbon nanotube composites: an overview. Materials *13*, 2771. https://doi.org/10.3390/ma13122771.

51. Molinari, R., Argurio, P., and Poerio, T. (2004). Comparison of polyethylenimine, polyacrylic acid and poly(dimethylamine-co-epichlorohydrin-co-ethylenediamme) in Cu^{2+} removal from wastewaters by polymer-assisted ultrafiltration. Desalination *162*, 217–228. https://doi.org/10.1016/s0011-9164(04)00045-1.

52. Jellouli Ennigrou, D., ben Sik Ali, M., and Dhahbi, M. (2014). Copper and Zinc removal from aqueous solutions by polyacrylic acid assisted-ultrafiltration. Desalination *343*, 82–87. https://doi.org/10.1016/j.desal.2013.11.006.

53. Chen, M., and Hankins, N.P. (2020). Interaction among branched polyethylenimine (PEI), sodium dodecyl sulfate (SDS) and metal cations during copper recovery from water using polymer-surfactant aggregates. J. Water Proc. Eng. *34*, 101170. https://doi.org/10.1016/j.jwpe.2020.101170.

54. Holyer, R.H., Hubbard, C.D., Kettle, S.F.A., and Wilkins, R.G. (1966). The kinetics of replacement reactions of complexes of the transition metals with 2, 2', 2''-terpyridine. Inorg. Chem. *5*, 622–625. https://doi.org/10.1021/ic50038a027.

55. Pakulski, D., Gorczyński, A., Marcinkowski, D., Czepa, W., Chudziak, T., Witomska, S., Nishina, Y., Patroniak, V., Ciesielski, A., and Samorì, P. (2021). High-sorption terpyridine–graphene oxide hybrid for the efficient removal of heavy metal ions from wastewater. Nanoscale *13*, 10490–10499. https://doi.org/10.1039/d1nr02255e.

56. Indumathy, R., Radhika, S., Kanthimathi, M., Weyhermuller, T., and Unni Nair, B. (2007). Cobalt complexes of terpyridine ligand: crystal structure and photocleavage of DNA. J. Inorg. Biochem. *101*, 434–443. https://doi.org/10.1016/j.jinorgbio.2006.11.002.

57. Wang, W., Sun, J., Zhang, Y., Zhang, Y., Hong, G., Moutloali, R.M., Mamba, B.B., Li, F., Ma, J., and Shao, L. (2022). Mussel-inspired tannic acid/polyethyleneimine assembling positively-charged membranes with excellent cation permselectivity. Sci. Total Environ. *817*, 153051. https://doi.org/10.1016/j.scitotenv.2022.153051.

58. Wang, H., Huang, K., Zhang, Y., Chen, X., Jin, W., Zheng, S., Zhang, Y., and Li, P. (2017). Recovery of lithium, nickel, and cobalt from spent lithium-ion battery powders by selective ammonia leaching and an adsorption separation system. ACS Sustain. Chem. Eng. *5*, 11489–11495. https://doi.org/10.1021/acssuschemeng.7b02700.

59. Ribeiro, A.C.F., Esteso, M.A., Lobo, V.M.M., Valente, A.J.M., Simões, S.M.N., Sobral, A.J.F.N., and Burrows, H.D. (2005). Diffusion coefficients of copper chloride in aqueous solutions at 298.15 K and 310.15 K. J. Chem. Eng. Data *50*, 1986–1990. https://doi.org/10.1021/je050220y.

60. Junker, M.A., de Vos, W.M., Lammertink, R.G., and de Grooth, J. (2021). Bridging the gap between lab-scale and commercial dimensions of hollow fiber nanofiltration membranes. J. Membr. Sci. *624*, 119100. https://doi.org/10.1016/j.memsci.2021.119100.

61. Woodward, I.R., Attia, L.M., Patel, P., and Fromen, C.A. (2021). Scalable 3D-printed lattices for pressure control in fluid applications. AIChE J. *67*, e17452. https://doi.org/10.1002/aic.17452.

62. Weidman, J.L., Mulvenna, R.A., Boudouris, B.W., and Phillip, W.A. (2015). Nanostructured membranes from triblock polymer precursors as high capacity copper adsorbents. Langmuir *31*, 11113–11123. https://doi.org/10.1021/acs.langmuir.5b01605.

63. Zhang, Y., Almodovar-Arbelo, N.E., Weidman, J.L., Corti, D.S., Boudouris, B.W., and Phillip, W.A. (2018). Fit-for-purpose block polymer membranes molecularly engineered for water treatment. npj Clean Water *1*, 2–14. https://doi.org/10.1038/s41545-018-0002-1.

64. Andres, P., Lunkwitz, R., Pabst, G., Böhn, K., Wouters, D., Schmatloch, S., and Schubert, U. (2003). New 4′-functionalized 2, 2′:6′, 2″-terpyridines for applications in macromolecular chemistry and nanoscience. Eur. J. Org. Chem. *2003*, 3769–3776. https://doi.org/10.1002/ejoc.200300327.

65. Dinic, J., Zhang, Y., Jimenez, L.N., and Sharma, V. (2015). Extensional relaxation times of dilute, aqueous polymer solutions. ACS Macro Lett. *4*, 804–808. https://doi.org/10.1021/acsmacrolett.5b00393.

66. Dinic, J., Jimenez, L.N., and Sharma, V. (2017). Pinch-off dynamics and dripping-onto-substrate (DoS) rheometry of complex fluids. Lab Chip *17*, 460–473. https://doi.org/10.1039/c6lc01155a.